International Journal of Computer Assisted Radiology and Surgery
https://doi.org/10.1007/s11548-018-1833-4

ORIGINAL ARTICLE

Modular force approximating soft robotic pneumatic actuator

Austin J. Taylor[1] · **Rudy Montayre**[1] · **Zhuo Zhao**[1] · **Ka Wai Kwok**[2] · **Zion Tsz Ho Tse**[1]

Received: 8 February 2018 / Accepted: 25 July 2018

Abstract

Purpose Soft robots are highly flexible and adaptable instruments that have proven extremely useful, especially in the surgical environment where compliance allows for improved maneuverability throughout the body. Endoscopic devices are a primary example of an instrument that physicians use to navigate to difficult-to-reach areas inside the body. This paper presents a modular soft robotic pneumatic actuator as a proof of concept for a compliant endoscopic device.

Methods The actuator is 3D printed using an FDM printer. Maximum bending angle is measured using image processing in MATLAB at a gauge pressure level of 35 psi. End-effector displacement is measured using electromagnetic tracking as gauge pressure ranges from 10 to 35 psi, and uniaxial tensile loading ranges from 0 to 120 g.

Results The actuator achieves a maximum bending angle of 145°. Fourth-order polynomial regression is used to model the actuator displacement upon inflation and tensile loading with an average coefficient of correlation value of 0.998. We also develop a feedforward neural network as a robust computer-assisted method for controlling the actuator that achieves a coefficient of correlation value of 0.996.

Conclusion We propose a novel modular soft robotic pneumatic actuator that is developed via rapid prototyping and evaluated using image processing and machine learning models. The curled resting shape allows for simple manufacturing and achieves a greater range of bending than other actuators of its kind. A feedforward neural network provides accurate prediction of end-effector displacement upon inflation and loading to deliver precise manipulation and control.

Keywords Soft robot · Image processing · Electromagnetic tracking · Neural network

Introduction

Endoscopes are widely used in diagnosis and treatment of human diseases to provide visualization of lesions within internal organs with high resolution [1, 2]. They can be inserted through natural body orifices to access internal organs, rather than through incision [3]. Both illumination and detection elements must be navigated through difficult anatomical pathways, requiring a combination of flexibility and stiffness [4]. A high degree of stiffness can lead to dangerous complications such as perforation of soft tissue or organs [5]. There is an enormous potential for research to improve the safety of instruments used to travel along complicated trajectories through the human anatomy. Soft robots offer a unique solution due to their inherent compliance and various actuation methods.

Soft robots have made a significant impact in the field of medical devices in applications ranging from wearable tactile-sensing materials [6–11] to implantable soft robotic devices [12, 13], to pneumatic actuators [14–18]. Inspired by biology, soft robots aim to actively and safely interact with their environment through high compliance [19–21]. Traditional, rigid-bodied robots are typically unsafe for human interaction and are designed to perform a single task efficiently, but often with limited adaptability. In contrast to rigid-bodied robots, soft robots have a continuously deformable structure, allowing them to better absorb the energy from a collision [22]. Soft robots exhibit unprecedented adaptation and sensitivity, making them ideal for navigating through confined spaces. Cianchetti et al. present a single-chamber soft robotic module for minimally invasive

---

✉ Zion Tsz Ho Tse
Ziontse@uga.edu

Austin J. Taylor
austintaylor@uga.edu

[1] School of Electrical and Computer Engineering, The University of Georgia, 597 DW Brooks Dr., Athens, GA 30602, USA

[2] Department of Mechanical Engineering, The University of Hong Kong, Pokfulam, Hong Kong, China

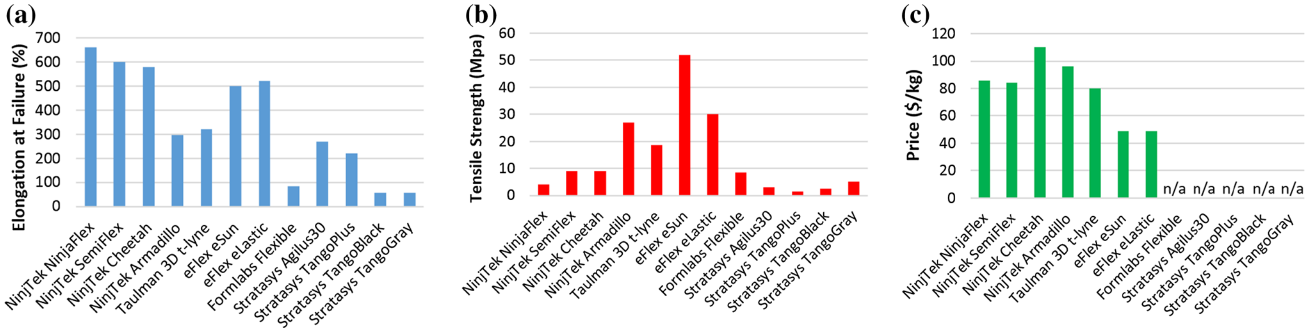

Fig. 1 3D printing filament specifications comparison. **a** Elongation at failure. **b** Tensile strength. **c** Price per kg

applications that produces 120° bending angle upon inflation [23]. The aim of this work is to explore various pneumatic actuator shapes to produce the maximum achievable bending angle with a single-chamber module.

In this study, we design and fabricate a modular, soft robotic pneumatic actuator for potential applications in endoscopy. The soft robot is actuated with air pressure, making it suitable for use in MRI. The actuator is fabricated quickly and economically with a fused deposition modeling (FDM) 3D printer, greatly reducing manufacturing time and cost. The actuator design comprises a curled resting position to achieve a greater bending angle upon actuation. It permits only one degree of freedom, but the modular design allows for multiple actuators to be connected in various configurations to achieve multiple degrees of freedom. The relationship between the actuator end-effector displacement, inflation pressure, and external forces is modeled via a polynomial regression and a feedforward neural network. End-effector displacement is measured via electromagnetic (EM) tracking, inflation pressure is measured via a pressure gauge, and external force is measured via manually applied loading. As this work is aimed at providing a proof of concept, practical safety concerns such as biocompatibility and sterilization are not evaluated. Future work will include biocompatibility design as well as modeling loading in various directions, distributed loading and torque.

Materials and methods

Modular soft robot design

The soft robotic actuator was designed using SolidWorks and 3D printed using a LulzBot Taz-6 printer. The LulzBot Taz-6 is an FDM 3D printer, and the printer filament is NinjaTek NinjaFlex, a thermoplastic polyurethane material. Various 3D printers and filaments were tested for comparison (Fig. 1), but ultimately NinjaFlex was chosen as the actuator material due to its superior flexibility. The advantage of high flexibility is that it allows for greater expansion of the fluidic chamber, resulting in a larger bending angle.

A key consideration in the design of the actuator was the ability to provide a maximum bending angle upon inflation. Typical soft robots are designed with a straight-line resting (deflated) shape, aimed at achieving multiple degrees of freedom using multiple inflation chambers. With the goal of achieving a maximum bending angle, our actuator design sacrifices the ability to have multiple degrees of freedom and embodies a curled resting shape (Fig. 2a), which is achieved by 3D printing the actuator in the curled shape. The curled resting shape allows for a greater range of bending in a single direction by utilizing the advantage of already being bent 180° in the resting position.

The relevant dimensions of the actuator are presented in Table 1. The actuator was printed using a layer height of 0.4 mm, but the overall size of the actuator can be miniaturized by reducing the layer height. For simplicity and uniformity, the wall thickness is constant throughout the entire actuator. The current dimensions of the actuator are not optimized for specific applications in minimally invasive surgery. The current work is a proof of concept aimed at evaluating the capabilities of the actuator for surgical applications. The optimization of the dimensions for a specific surgical procedure is outside the scope of this article.

Male and female connection components were incorporated into opposite ends of the actuator to enable a modular design. The fluidic chamber does not enter the joint components, making the joints unaffected by inflation. The design of the joint allows for two actuators to be connected to each other in four different configurations, each offset by 90° rotation from each other, permitting the configuration to achieve multiple degrees of freedom. The joints are designed to connect to each other by creating a tight fitting between the male and female parts and can withstand a maximum tensile load of 14 N without disconnecting. The actuator contains a single air inlet (Fig. 2a, c). Figure 2b shows a 3D printed actuator, and Fig. 2c shows the cross-sectional view of the actuator as well as the direction of actuation. Figure 2d–f displays various possible configurations for connecting multiple actuators.

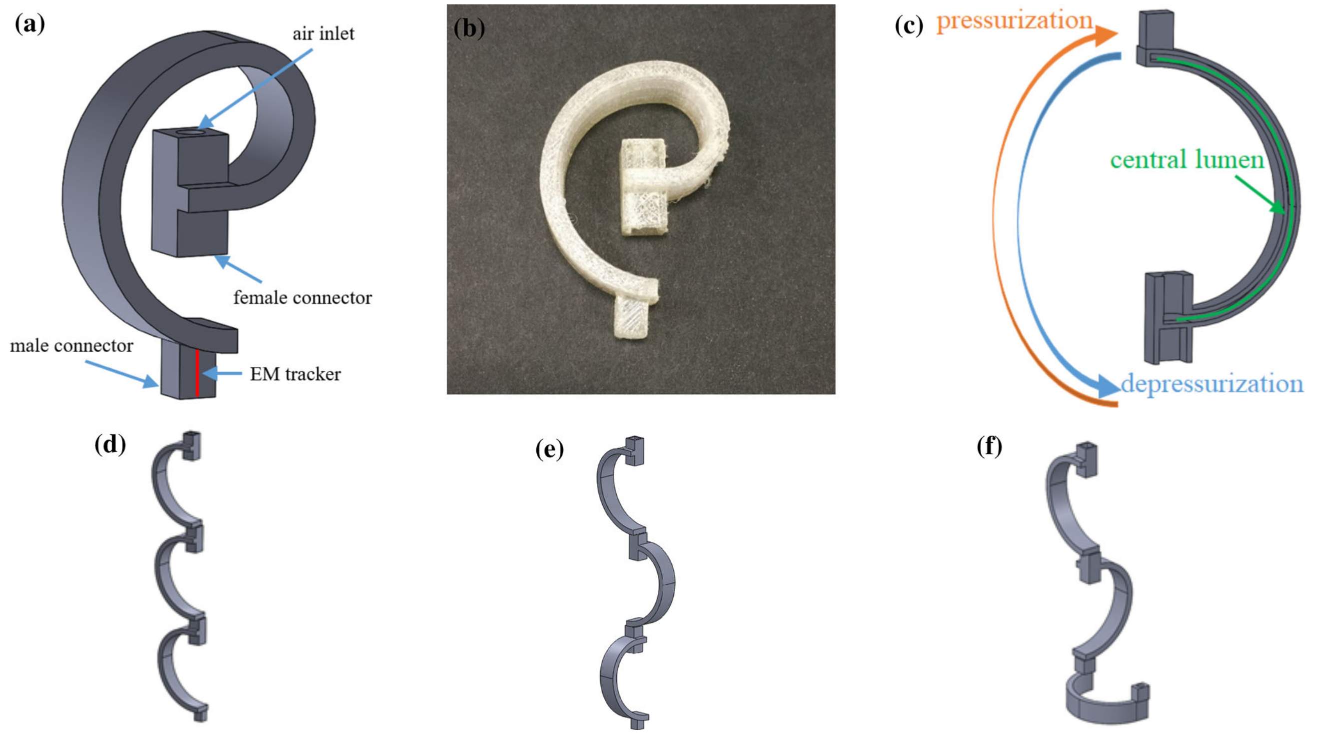

Fig. 2 **a** CAD model of actuator deflated; **b** 3D printed actuator; **c** CAD model of actuator inflated, cross-sectional view; **d**–**f** three potential configurations for 3-link structures

Table 1 Dimensions of the actuator

Deflated height, length, width	Inflated height, length, width	Wall thickness	Fluidic chamber volume	Air inlet diameter
$45 \times 30 \times 10$ mm	$60 \times 26.5 \times 10$ mm	0.8 mm	884 mm^3	3.6 mm

Static model of the soft robot with image processing

A MATLAB program was developed to model the curvature of the actuator based on processed images of the actuator under various gauge pressure levels so that the repeatability and maximum bending angle could be accurately measured. The actuator was held with a clamp upright (gravity loaded) at the base of the actuator during the experiment and images were taken with the actuator deflated and fully inflated (Fig. 3a, d). The images were processed in MATLAB with the edge detection feature to create a trace of the outline of the actuator (Fig. 3b, e). The inside arc of the trace was reconstructed by splitting the arc into six segments, estimating the curvature of each segment using the arc radius Eq. (1), and splicing the resulting segments together (Fig. 3c, f). The arc radius equation is a manipulation of the intersecting chords theorem (Fig. 4). The intersecting chords theorem states that when two chords intersect each other inside a circle, the products of their segment lengths are equal (Fig. 5a). If one of the intersecting chords bisects the other chord, the intersecting chords theorem can be used to derive the arc radius equation (Fig. 5b).

The length of the chord, l, and the length of the segment between the center point of the arc and the midpoint of the chord, labeled h, are the only needed values to calculate the arc radius, R.

$$R = \frac{4h^2 + l^2}{8h} \tag{1}$$

A starting point (x_s, y_s), an endpoint (x_e, y_e), and a center point (x_c, y_c) were manually selected for each of the six segments s_n, totaling 18 (x, y) coordinate points for approximating the curvature.

$$s_n = \begin{bmatrix} x_\mathrm{s} & y_\mathrm{s} \\ x_\mathrm{e} & y_\mathrm{e} \\ x_\mathrm{c} & y_\mathrm{c} \end{bmatrix} \tag{2}$$

After developing a model for the curvature, the performance of the actuator was evaluated by measuring the repeatability and the maximum bending angle resulting from full inflation.

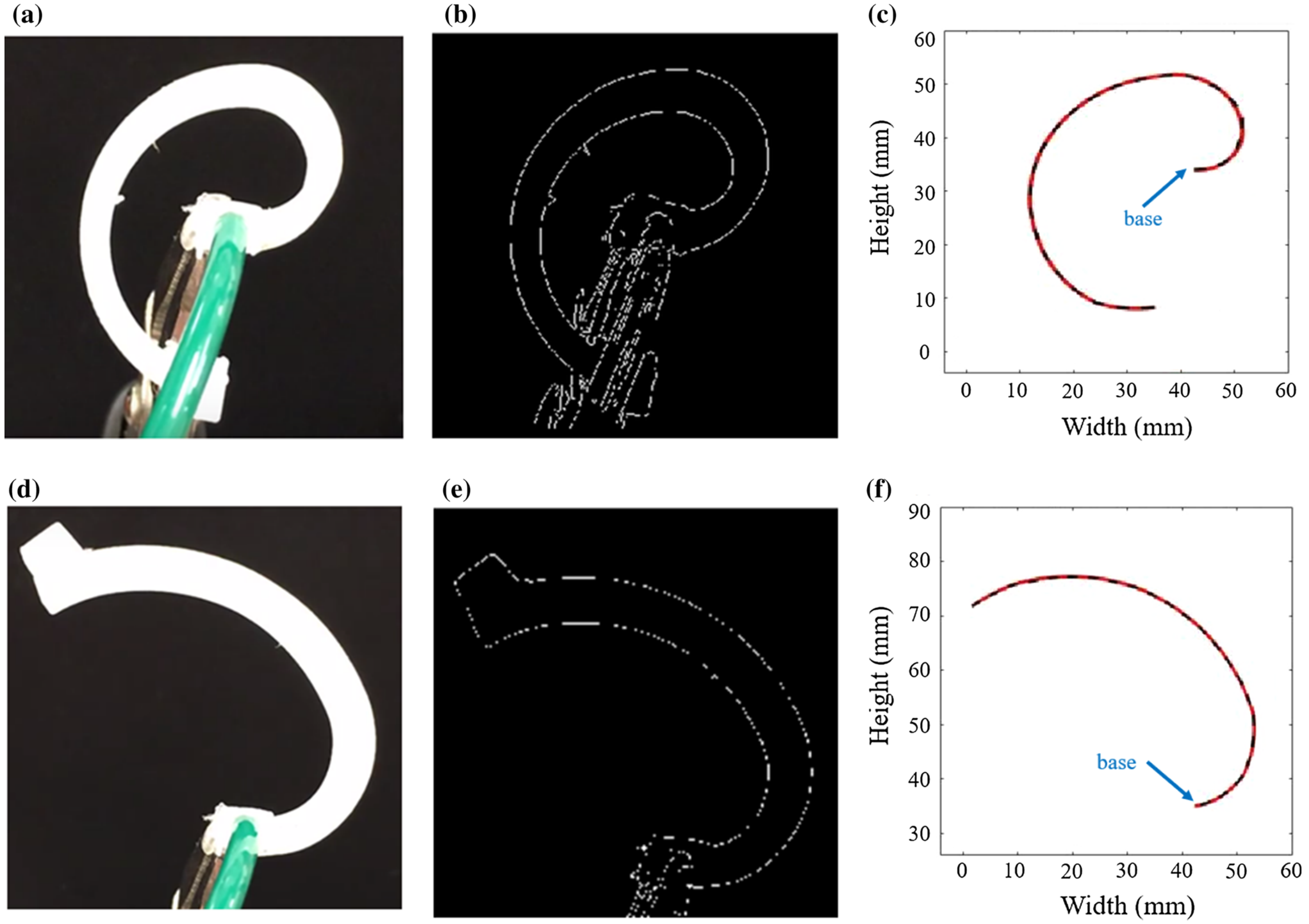

Fig. 3 Experimental setup and image processing via MATLAB: **a** deflated actuator photo; **b** deflated actuator image processing; **c** deflated actuator inner arc reconstruction; **d** inflated actuator photograph; **e** inflated actuator image processing; **f** inflated actuator inner arc reconstruction

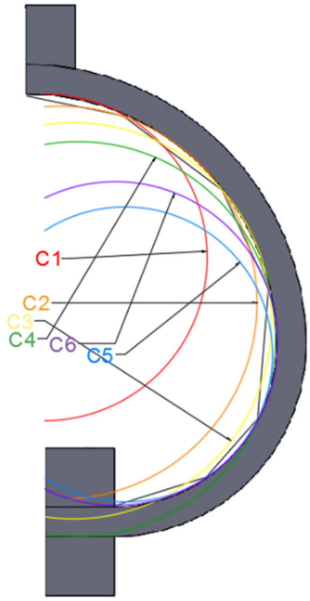

Fig. 4 Inner curvature of soft robotic actuator approximated by dividing the arc into six segments and calculating the radius of each segment

Electromagnetic tracking-based force approximation

The actuator was placed under various tensile loading and gauge pressures to understand and predict the end-effector displacement behavior. To quickly and accurately track the displacement of the end effector upon loading, the actuator was equipped with a Northern Digital Inc. (NDI) five-degree-of-freedom EM tracking sensor. An Aurora V3 Planar Field Generator was used to generate a magnetic field to track the sensor. The EM sensor was mounted to the end effector of the actuator and connected to the Aurora Sensor Interface Unit and System Control Unit. EM tracking was conducted in a 500 mm × 500 mm × 500 mm working volume located 50 mm away from the front of the Aurora field generator (Fig. 6). The actuator was mounted at the air inlet location as shown in Fig. 3a, allowing the opposite end to move freely. A uniaxial tensile load was applied vertically downward by hanging weights from the end effector of the actuator. The actuator displacement was measured at various gauge pressures ranging from 10 to 35 psi in increments of 5 psi and at

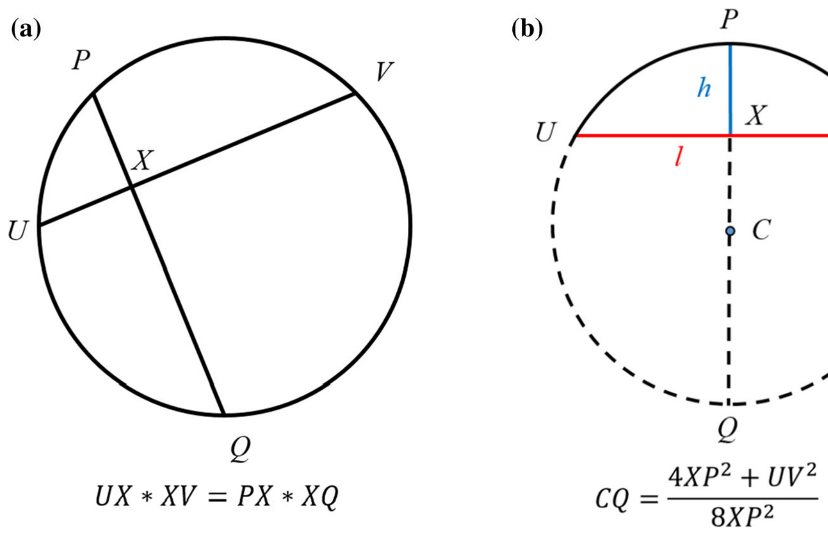

Fig. 5 **a** Diagram showing the intersecting chords theorem; **b** diagram showing the derivation of the arc radius equation

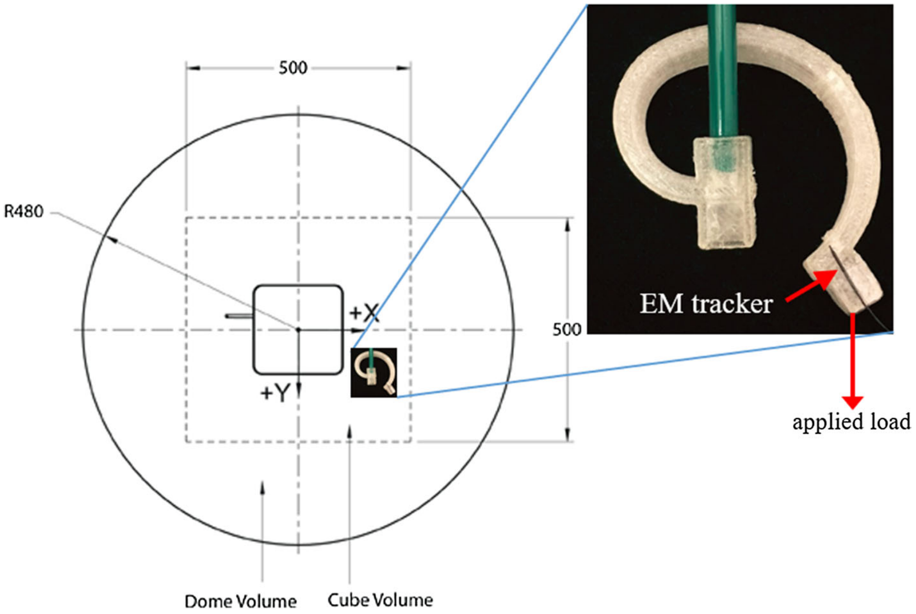

Fig. 6 Diagram depicting the actuator in Aurora magnetic field [24]. Values are expressed in millimeters. The red arrows indicate the location of the EM tracker and the direction of the applied load

various loads ranging from 0 to 120 g in increments of 10 g. All displacements reported are maximum displacement. The time taken to achieve maximum displacement was also measured and reported.

Feedforward neural network

The EM tracking displacement data were fed into a single-layer feedforward neural network in MATLAB. Three sets of the displacement data were collected at each combination of gauge pressure and tensile loading for a total of 234 data points. A randomly selected 70% of the data was used to train the neural network, 15% of the data was used as a validation set, and 15% was used as a test set. The network architecture consists of two inputs (inflation pressure, load), a single hidden layer with four units, and an output layer with a single linear activation (displacement). The network was trained using the Levenberg–Marquardt algorithm until the validation error stopped improving, thus preventing overfitting.

Results and discussion

Actuator performance evaluation

The performance of the actuator was evaluated by measuring the repeatability and the maximum bending angle. The end-effector displacement (mm) was measured at 5-psi intervals ranging from 10 to 35 psi using the arc radius curvature model. The repeatability was evaluated by computing the

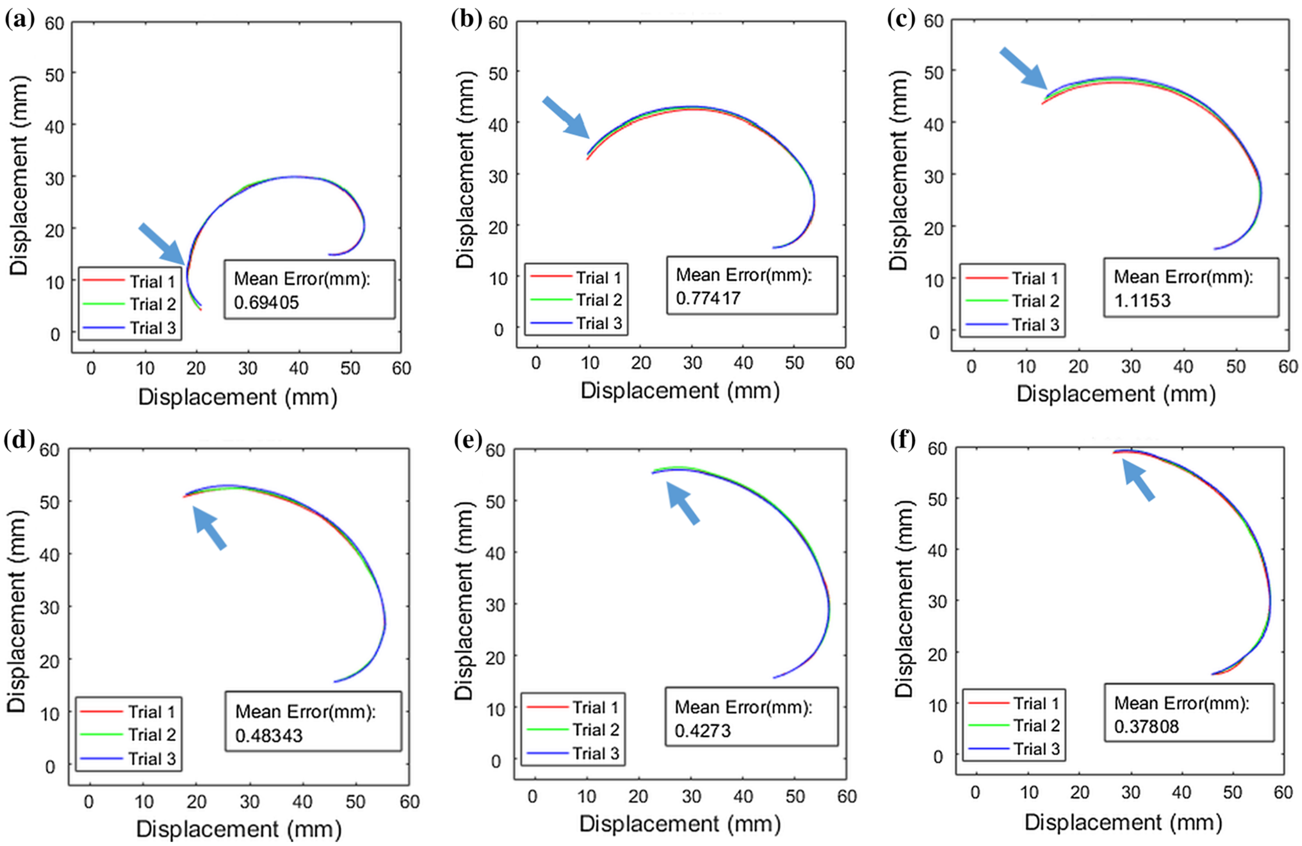

Fig. 7 Plot showing the repeatability of the tip displacement upon inflation. Blue arrows show the position of the actuator tip under gauge pressure levels from 10 to 35 psi; **a** 10 psi, **b** 15 psi, **c** 20 psi, **d** 25 psi, **e** 30 psi, **f** 35 psi

mean error of the end-effector displacement of three different trials at each pressure level for a single actuator (Fig. 7). The results show an error of less than 1.2 mm at each of the six different pressure levels, demonstrating that the actuator can be accurately controlled by regulating the gauge pressure. The maximum bending angle achieved for a single actuator was 145° with an applied gauge pressure of 35 psi. This is a greater maximum bending angle than most other pneumatic actuators in the literature, without the need for a crimped external shell [23] or fiber reinforcement [18].

EM tracking repeatability analysis

The repeatability of the EM tracker was determined by computing the mean error of the end-effector displacement (mm) of ten different trials at each gauge pressure level for a single actuator. Figure 8 displays the mean displacement error of the ten different trials for each gauge pressure level, with error bars displaying the standard deviation. The maximum mean displacement error was approximately 0.47 mm with a standard deviation of less than 0.1 mm, validating the repeatability of the EM tracking method.

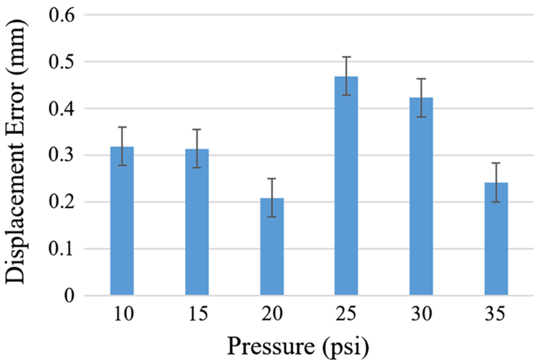

Fig. 8 Mean displacement error of ten trials for each gauge pressure level with error bars displaying the standard deviation

Polynomial regression model

The ability of the soft robotic actuator to withstand tensile loading was modeled using a fourth-order polynomial regression model. The regression model is presented in Fig. 9, and the parameter values are listed in Table 2. The model shows a significant change in the behavior and overall displacement in the actuator when the applied load is greater than 50 g (0.5 N). The model yielded an average coefficient of correla-

Fig. 9 Fourth-order polynomial regression of pressure versus displacement as the load varies from 0 to 120 g (0–1.18 N)

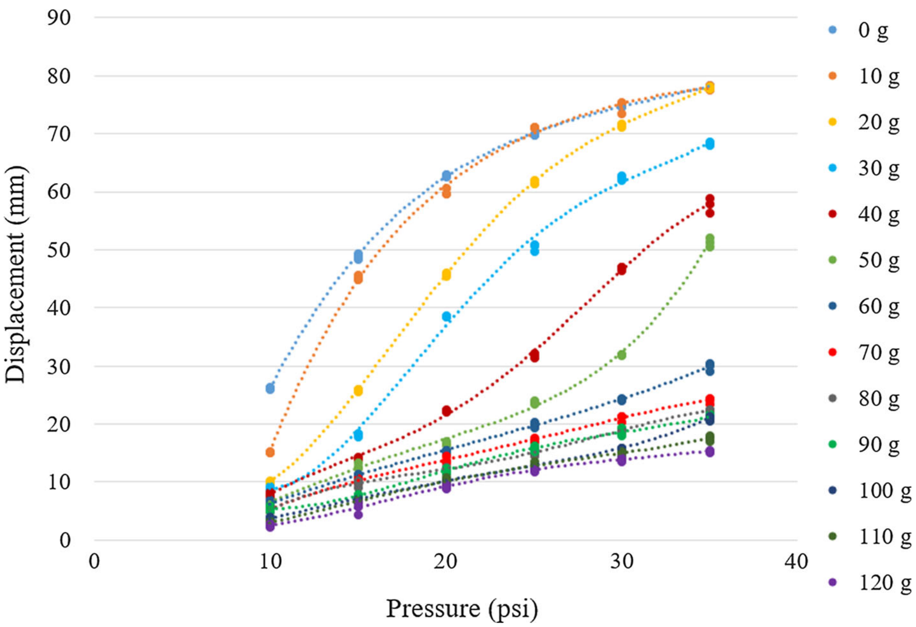

Table 2 Fourth-order polynomial regression model parameter values

Weight (g)	β_0	β_1	β_2	β_3	β_4
0	−65.571	13.275	−0.4855	0.0081	−0.00005
10	−116.26	20.082	−0.853	0.0174	−0.0001
20	47.904	−12.38	1.1772	−0.0353	0.0004
30	85.079	−19.113	1.5518	−0.0448	0.0004
40	−41.872	10.161	−0.7504	0.0261	−0.0003
50	−2.8065	0.0911	0.1498	−0.008	0.0001
60	−7.519	1.7332	−0.0418	0.0006	0.00006
70	−18.532	4.0303	−0.2221	0.0064	−0.00007
80	−30.602	6.7933	−0.4358	0.0129	−0.0001
90	25.857	−4.9997	0.399	−0.01115	0.0001
100	0.9713	−0.4197	0.1071	−0.0044	0.00006
110	−0.7429	−0.2418	0.0914	−0.0034	0.00004
120	7.8102	−1.991	0.202	−0.0063	0.00007

tion value, R, of 0.99834. The time taken to achieve maximum displacement for each of the reported measurements was on average 0.4 s.

Feedforward neural network

The performance of the neural network was measured by evaluating the mean-squared error (MSE) between the output displacement values and the target displacement values. The model obtained a MSE of 1.2788 mm on the validation set at the 22nd epoch (Fig. 10). The coefficient of correlation value, R, was 0.99639 for the training set, 0.99471 for the validation set, 0.99737 for the test set, and 0.99643 overall (Fig. 11). In comparison with the polynomial regression model, the neural network performed worse by 0.2%. Although the neural network performed slightly worse than the polynomial regression, it is a robust computer-assisted method for controlling the actuator that can easily scale with larger datasets and additional features.

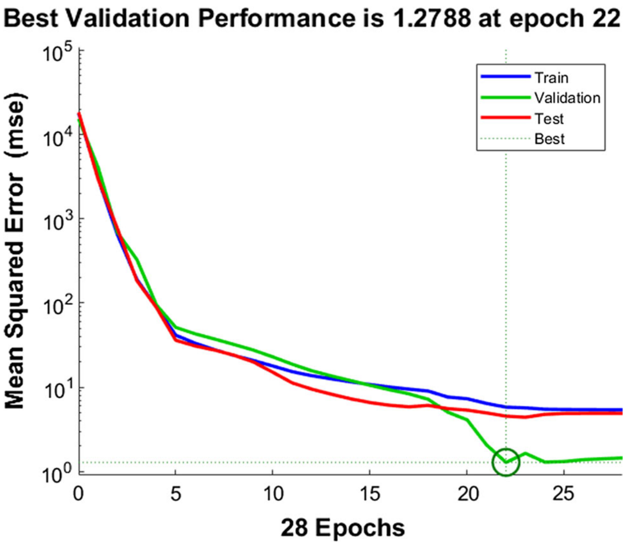

Fig. 10 Neural network performance evaluation

Conclusion

This study presents the development of a modular pneumatic soft robotic actuator that can be used to form a multi-degree-of-freedom steerable mechanism for potential applications in MIS. The proposed actuator is 3D printed in under 1 h

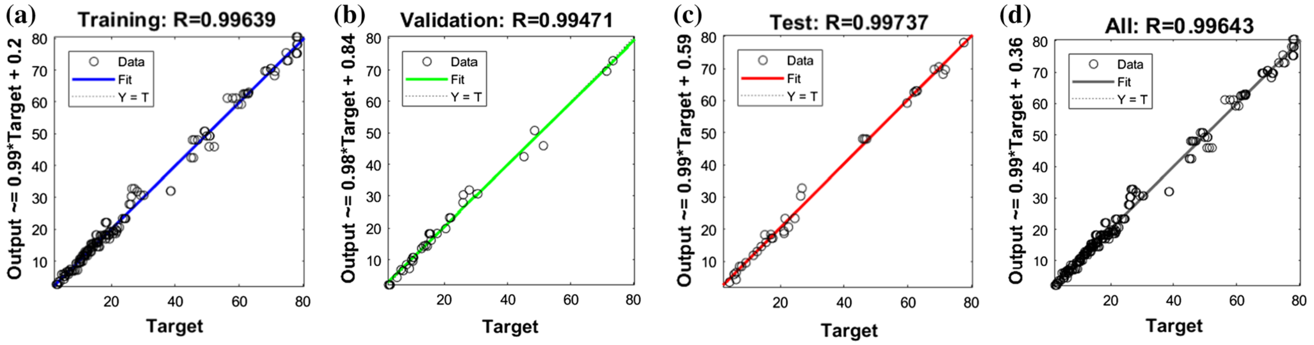

Fig. 11 Neural network regression analysis: **a** training set, **b** validation set, **c** test set, **d** training, validation and test data combined

and costs less than one US dollar. The curled design of the actuator achieves a greater maximum bending angle upon actuation than other pneumatic actuators reported in the literature. The intersecting chords theorem is applied to develop a mathematical model of the actuator that is used to measure the bending performance and the repeatability. An EM tracker is attached to the distal end of the actuator and used to track the end-effector position as various loads are applied. We develop a fourth-order polynomial regression model to show the relationship between the load, the inflation pressure, and the end-effector displacement. Finally, we develop a feedforward neural network model to control the actuator. The modular soft robotic actuator presented in this work is an extremely low-cost approach for constructing complex multi-degree-of-freedom soft robotic systems. As this work is aimed at providing a proof of concept, practical safety concerns such as biocompatibility and sterilization are not evaluated. Future work will include biocompatibility design as well as modeling multiaxial loading, distributed loading, and torque.

Acknowledgments This study was supported in part by the National Institutes of Health (NIH) Bench-to-Bedside Award, the NIH Center for Interventional Oncology Grant, the National Science Foundation (NSF) I-Corps Team Grant (1617340), NSF REU site program 1359095, the UGA-AU Inter-Institutional Seed Funding, the American Society for Quality Dr. Richard J. Schlesinger Grant, the PHS Grant UL1TR000454 from the Clinical and Translational Science Award Program, and the NIH National Center for Advancing Translational Sciences.

Compliance with ethical standards

Conflict of interest The authors declare that they have no conflict of interest.

Ethical approval This article does not contain any studies with human participants or animals performed by any of the authors.

Informed consent This article does not contain patient data.

References

1. Elahi SF, Wang TD (2011) Future and advances in endoscopy. J Biophotonics 4(7–8):471–481
2. Seibel EJ, Johnston RS, Melville CD (2006) A full-color scanning fiber endoscope. In: Optical fibers and sensors for medical diagnostics and treatment applications VI, vol 6083. International Society for Optics and Photonics, p 608303
3. Moore JE Jr, Maitland DJ (2013) Biomedical technology and devices. CRC Press, Boca Raton
4. Lee CM, Engelbrecht CJ, Soper TD, Helmchen F, Seibel EJ (2010) Scanning fiber endoscopy with highly flexible, 1 mm catheterscopes for wide-field, full-color imaging. J Biophotonics 3(5–6):385–407
5. Lippert E, Herfarth HH, Grunert N, Endlicher E, Klebl F (2015) Gastrointestinal endoscopy in patients aged 75 years and older: risks, complications, and findings—a retrospective study. Int J Colorectal Dis 30(3):363–366
6. Lu N, Kim D-H (2014) Flexible and stretchable electronics paving the way for soft robotics. Soft Robot 1(1):53–62
7. Trung TQ, Lee NE (2016) Flexible and stretchable physical sensor integrated platforms for wearable human-activity monitoringand personal healthcare. Adv Mater 28(22):4338–4372
8. Gao Y, Ota H, Schaler EW, Chen K, Zhao A, Gao W, Fahad HM, Leng Y, Zheng A, Xiong F (2017) Wearable microfluidic diaphragm pressure sensor for health and tactile touch monitoring. Adv Mater 29(39):1701985
9. Shimoga KB, Goldenberg AA (1992) Soft materials for robotic fingers. In: 1992 IEEE international conference on robotics and automation, 1992. Proceedings. IEEE, pp 1300–1305
10. Dahiya RS, Metta G, Valle M, Sandini G (2010) Tactile sensing—from humans to humanoids. IEEE Trans Rob 26(1):1–20
11. Polygerinos P, Wang Z, Galloway KC, Wood RJ, Walsh CJ (2015) Soft robotic glove for combined assistance and at-home rehabilitation. Rob Auton Syst 73:135–143
12. Payne CJ, Wamala I, Abah C, Thalhofer T, Saeed M, Bautista-Salinas D, Horvath MA, Vasilyev NV, Roche ET, Pigula FA (2017) An implantable extracardiac soft robotic device for the failing heart: mechanical coupling and synchronization. Soft Robot 4(3):241–250
13. Van Story D, Saeed M, Price K, Wamala I, Hammer PE, Bautista-Salinas D, Vogt DM, Walsh CJ, Wood RJ, Vasilyev NV (2017) Approaches to real-time ventricular wall strain measurement for the control of soft robotic ventricular assist devices
14. Noritsugu T, Yamamoto H, Sasakil D, Takaiwa M (2004) Wearable power assist device for hand grasping using pneumatic artificial rubber muscle. In: SICE 2004 annual conference, 2004, vol 1. IEEE, pp 420–425

15. Noritsugu T (2005) Pneumatic soft actuator for human assist technology. In: Symposium on fluid power, vol 2005
16. Connelly L, Jia Y, Toro ML, Stoykov ME, Kenyon RV, Kamper DG (2010) A pneumatic glove and immersive virtual reality environment for hand rehabilitative training after stroke. IEEE Trans Neural Syst Rehabil Eng 18(5):551–559
17. Klute GK, Czerniecki JM, Hannaford B (1999) McKibben artificial muscles: pneumatic actuators with biomechanical intelligence. In: IEEE/ASME international conference on advanced intelligent mechatronics, 1999. Proceedings. IEEE, pp 221–226
18. Bishop-Moser J, Krishnan G, Kim C, Kota S (2012) Design of soft robotic actuators using fluid-filled fiber-reinforced elastomeric enclosures in parallel combinations. In: IEEE/RSJ international conference on intelligent robots and systems (IROS), 2012. IEEE, pp 4264–4269
19. Kim S, Laschi C, Trimmer B (2013) Soft robotics: a bioinspired evolution in robotics. Trends Biotechnol 31(5):287–294
20. Trimmer BA, Lin H-T, Baryshyan A, Leisk GG, Kaplan DL (2012) Towards a biomorphic soft robot: design constraints and solutions. In: 4th IEEE RAS & EMBS international conference on biomedical robotics and biomechatronics (BioRob), 2012. IEEE, pp 599–605
21. Pfeifer R, Lungarella M, Iida F (2012) The challenges ahead for bio-inspired ‘soft’ robotics. Commun ACM 55(11):76–87
22. Rus D, Tolley MT (2015) Design, fabrication and control of soft robots. Nature 521(7553):467
23. Cianchetti M et al (2014) Soft robotics technologies to address shortcomings in today’s minimally invasive surgery: the STIFF-FLOP approach. Soft Robot 1(2):122–131
24. NDI Medical (2017) Aurora. https://www.ndigital.com/medical/products/aurora/